



Morphology Defined ZnO Nanostructures Through Microwave Assisted Chemical Synthesis: Growth Mechanism, Defect Structure, and Emission Behaviours

Ma. de Lourdes Ruiz Peralta¹, J. García Serrano², and U. Pal^{1,*}

¹*Instituto de Física, Universidad Autónoma de Puebla, Apdo. Postal J-48, Puebla, Pue. 72570, Mexico*

²*Instituto de Ciencias Básicas e Ingeniería, Universidad Autónoma de Estado de Hidalgo, C.U., Carretera Pachuca-Tulancingo Km. 4.5, Hidalgo 42184, Mexico*

Zinc oxide nanostructures of rod, twisted-needle, petals and flower-like morphologies could be grown by microwave assisted chemical synthesis with excellent reproducibility. Each of the morphologies evolved through controlling the pH of the reaction mixture in between 5.5 and 12.0 before microwave irradiation. Morphology, structural, optical and optoelectronic properties of the nanostructures have been studied using scanning electron microscopy, transmission electron microscopy, X-ray diffraction, micro-Raman spectroscopy and photoluminescence spectroscopy. It has been observed that both the crystallinity and defect structures in the nanostructures depend strongly on synthesis conditions. Mechanisms of morphology evolution and photoluminescence emission behaviours of the nanostructures are presented.

Keywords: ZnO Nanostructures, Microwave Irradiation, Morphology Control, Defect Structure, PL Emission.

1. INTRODUCTION

Zinc oxide is a wide band gap (3.37 eV at 300K) semiconductor with large exciton binding energy (60 meV)¹ with diverse applications ranging from optoelectronic devices like light-emitting diodes,² solar cells,³ Schottky diodes,⁴ to chemical catalysis.⁵ The control over size and morphology in semiconductors of nanometer and micrometer dimensions presents a real challenge for the design of novel functional devices. Depending on the synthesis techniques, ZnO nanostructures with different morphologies like needles,⁶ rods,^{7,8} flowers,⁹ and belts,¹⁰ have been synthesized. However, one dimensional (1-D) nanostructures like nanowires and nanorods have received special attention due their applications as efficient gas sensors,^{11–13} photocatalysts,¹⁴ and intracellular nanosensors.¹⁵ On the other hand, ZnO nanostructures of different morphologies have been tried to fabricate hybrid (organic-inorganic) and dye-sensitized solar cells (DSSCs). For example, Beek et al.¹⁶ have utilized ZnO nanoparticles of 5.0 nm average diameter to blend with poly[2-methoxy-5-(3',7'-dimethyloctyloxy)-1,4-phenylenevinylene] (MDMO-PVP) to produce hybrid photovoltaic cells with high fill factor and open circuit voltage. Jiang et al.¹⁷ have utilized ZnO nanoflowers as

photoanode in DSSCs and revealed their higher solar conversion efficiency than ZnO nanowires. On the other hand, Cheng et al.¹⁸ have utilized ZnO microflowers of hierarchical morphologies to fabricate quasi-solid state DSSCs of efficiency as high as 4.12%. Guillén et al.¹⁹ could obtain DSSCs of 2.9% efficiency utilizing commercial ZnO nanoparticles and non-volatile ionic electrolytes of low-viscosities. Though the fabrication of those hybrid and dye-sensitized solar cells have been performed with inorganic ZnO nanostructures of different sizes and morphologies, using different organic dyes and solvents,²⁰ it is expected that the solar conversion efficiency of the fabricated devices would depend strongly on the specific surface area and hence the morphology of the nanostructures. Therefore, a general method for fabricating ZnO nanostructures of different morphologies and dimensions is essential for their applications in solar cells. On the other hand, before applying those nanostructures in devices like DSSC it is essential to evaluate their crystallinity, and defect structures.

A large number of physical or chemical methods have been adopted for the synthesis of ZnO nanostructures. Most of the exotic morphologies of ZnO have been grown using physical techniques like chemical vapor deposition (CVD),²¹ molecular beam epitaxy (MBE),²² and sputtering.²³ Nevertheless, wet-chemical routes^{24,25} are preferred for the production of ZnO as

* Author to whom correspondence should be addressed.

they use low growth temperature, produce large area deposition, lower reaction time, and of low production cost.^{26, 27}

Microwave assisted chemical bath deposition (MW-CBD) technique; based on microwave irradiation of precursors in solution has been reported²⁸ for the production of nanostructured metal oxide thin films with different morphologies. Though a microwave-enhanced reaction mechanism is not yet unveiled, the technique is advantageous to induce localized high temperature at reaction sites, enhancing the reaction rate,²⁹ and shortening the growth time. Recently, MW assisted chemical synthesis has been used to produce ZnO nano- and microstructures of different morphologies,^{25–34} using aqueous and non-aqueous media. Evolutions of sample morphology, doping efficiency, and defect structure of those low-dimensional ZnO structures have also been studied to some extent.

In this work, we report on the fabrication of rod, twisted-needle, petals, and flower-like ZnO nanostructures by MW-assisted chemical synthesis with excellent reproducibility. The ZnO nanostructures were characterized by X-ray diffraction (XRD), scanning electron microscopy (SEM), micro-Raman spectroscopy, and photoluminescence (PL) spectroscopy. Effects of solution pH on the morphology, structure, and optoelectronic properties of the nanostructures have been studied. Mechanisms of formation of the nanostructures are proposed.

2. EXPERIMENTAL DETAILS

For synthesizing ZnO nanostructures, first a 160 ml equimolar aqueous solutions of zinc nitrate hexahydrate [$\text{Zn}(\text{NO}_3)_2 \cdot 6\text{H}_2\text{O}$, J. T. Baker, 99%] (0.008 M) and hexamine [HMT, $\text{C}_6\text{H}_{12}\text{N}_4$, Sigma-Aldrich, 99%] were prepared under vigorous magnetic stirring for 30 min. Two solutions were mixed together, and the final pH of the mixture was adjusted by drop-wise addition of 1.0 M sodium hydroxide [NaOH, Sigma-Aldrich, 99%] solution. Four reaction mixtures were prepared with final pH values 5.5, 8.0, 10.0, and 12.0. After that, the solutions in glass beakers were introduced (one at a time) into a domestic microwave oven (LG, model SVMS 0745VS) and irradiated for 10 minutes with 475 W microwave power. The microwave oven operated with 10 seconds on and 10 seconds off modes. The irradiation process was repeated for 5 cycles with about 10 min pause after each cycle. The maximum temperature of the irradiated reaction mixture reached to 95 °C. Formation of white precipitate in the microwave irradiated reaction mixture indicated the formation of ZnO. After the 5 cycles of microwave irradiation, the reaction mixtures were cooled to room temperature, and the white precipitates were separated through centrifuging. The collected samples were washed by centrifuging using ethanol and deionized (DI) water several times. After that, the samples were dried at room temperature to get white powders. Each of the samples was synthesized at least 5 times to check their morphological reproducibility.

For analyzing the structural and morphological characteristics of the obtained samples, a Bruker Discover D-8 X-ray diffraction (XRD) unit with $\text{CuK}\alpha$ radiation ($\lambda = 1.5406 \text{ \AA}$) source and a JEOL JSM6610LV field emission scanning electron microscope (FESEM) attached with a INCA Oxford analytical system were used. For high resolution transmission electron microscopy, the samples dispersed in ethanol were placed over carbon coated copper grids, dried, and observed using a JEOL 2010 FEG microscope operating at 200 kV. Raman spectra of the ZnO samples

were recorded at room temperature (RT) using an OLYMPUS BX41 microRaman system of Horiba JobinIvon, fitted with a He-Ne (332.6 nm) laser as excitation source and a thermoelectrically cooled ($-68.0 \text{ }^\circ\text{C}$) charged couple device as detector. Photoluminescence (PL) spectra of the powder samples were recorded at RT using the 325 nm emission of a He-Cd laser (Melles-Griot) as excitation sources and a thermoelectrically cooled Hamamatsu (PMH-04) photomultiplier as detector. A computer controlled 80 cm long ScienceTech monochromator with 1200 lines/cm ruled holographic grating was used to record the PL spectra.

3. RESULTS AND DISCUSSION

XRD patterns of the as-grown ZnO samples (in powder form) are presented in Figure 1. As can be seen, the sample prepared at pH = 5.5 (without adding NaOH solution) revealed sharp diffraction peaks correspond to the hexagonal wurtzite phase of ZnO, matching well with the standard XRD data file (JCPDS card no.36-1451). In general, on increasing the pH of the reaction mixture, the intensity of the diffraction peaks decreased, indicating a loss of crystallinity. The grain/crystallite size in the samples was estimated using the Scherrer relation on the most intense (101) diffraction peak:

$$p = \frac{0.9\lambda}{\beta \cos \theta} \quad (1)$$

where p is the average crystallite size, λ (1.5406 \AA) is the wavelength of the X-ray beam, β is the full width at half maximum (FWHM) of the diffraction peak in radians, and θ is the Bragg angle.

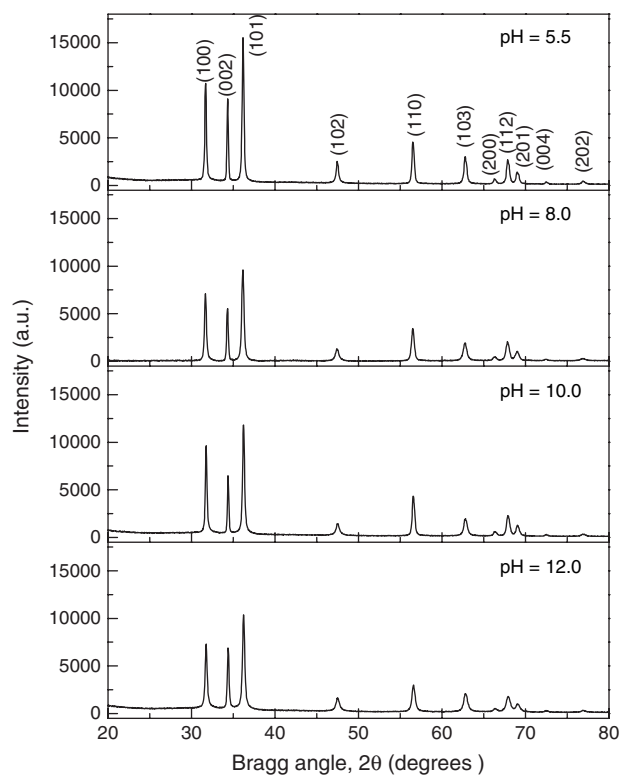


Fig. 1. XRD patterns of the ZnO nanostructures synthesized at different pH values of the reaction mixture.

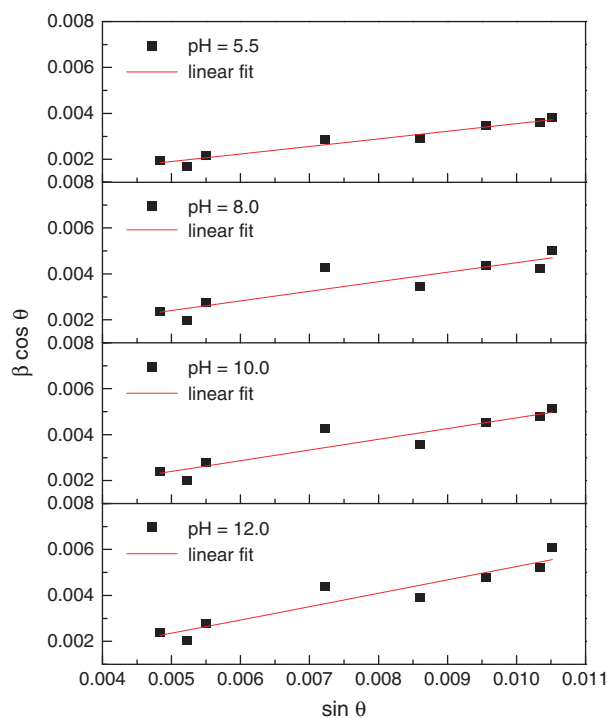


Fig. 2. Williamson-Hall ($\beta \cos \theta$ vs. $\sin \theta$) plots for the ZnO nanostructures synthesized at different pH values of the reaction mixtures.

To estimate the effect of pH of the reaction mixture on lattice deformation, the microstrain in the samples was estimated using the Williamson-Hall relation:

$$\beta \cos \theta = \frac{K\lambda}{p} + \varepsilon \sin \theta \quad (2)$$

where K is the form factor, assumed to be 0.90, and ε is the microstrain. Through $\beta \cos \theta$ versus $\sin \theta$ plots (Fig. 2), lattice microstrains in the samples were estimated. In Table I, the average crystallite size, microstrain, and EDS composition (in at. %) of all the samples are presented. As can be observed, on increasing the pH of the reaction mixture, crystallite size of the samples decreases and microstrain in the crystal lattice increases. Such an increase in microstrain indicates an increase of tensile strain in the ZnO lattice on increasing the pH of the reaction mixture. On the other hand, by changing the reaction solution from acidic to basic, the Zn/O atomic ratio in the samples decreases.

Typical SEM micrographs of the samples presented in Figure 3 clearly demonstrate the variation of sample morphology on the pH of the reaction mixture. As can be observed, the sample prepared with acidic reaction mixture (pH = 5.5) generates rod-like nanostructures. On increasing the pH of the reaction mixture

Table I. Crystallite size, microstrain (ε), and chemical composition of the ZnO nanostructures obtained using Scherrer formula, Williams-Hall plots, and EDS analysis, respectively.

pH of the reaction mixture	Crystallite size (nm)	ε	Zn (at. %)	O (at. %)
5.5	66.2	0.330	48.26	51.76
8.0	55.0	0.416	45.86	54.14
10.0	54.2	0.467	45.82	54.18
12.0	53.1	0.581	44.42	55.58

Table II. Typical morphologies of the ZnO nanostructures obtained for different pH values of the reaction mixture.

Reaction temperature (°C)	pH of the reaction mixture	Observed morphology	Average dimension (L = length; D = diameter/width)
95 ± 2	5.5	Faceted rods	$L = 3.2 \mu\text{m}$, $D = 0.5 \mu\text{m}$
95 ± 2	8.0	Petals/spindles	$L = 3.0 \mu\text{m}$, $D = 0.5 \mu\text{m}$
95 ± 2	10.0	Twisted needles	$L = 3.7 \mu\text{m}$, $D = 0.5 \mu\text{m}$
95 ± 2	12.0	Flower-like	L (petals) = $0.85 \mu\text{m}$, $D = 0.7 \mu\text{m}$

from 5.5 to 8.0, the rod-like morphology of the ZnO nanostructures changes to petal/spindle-like. On increasing the pH of the reaction mixture to 10.0, the morphology of the ZnO nanostructures becomes twisted needle-like. However, a drastic change in morphology is observed when the pH of the reaction mixture was set to 12.0. For this pH value, the morphology of the ZnO nanostructures became flower-like, with several petals coming out of a common stem. As the reaction temperature, concentrations of zinc acetate and HMT remained fixed for all the samples, the observed morphology evolution of the ZnO nanostructures is believed to be solely due to the variation of the pH

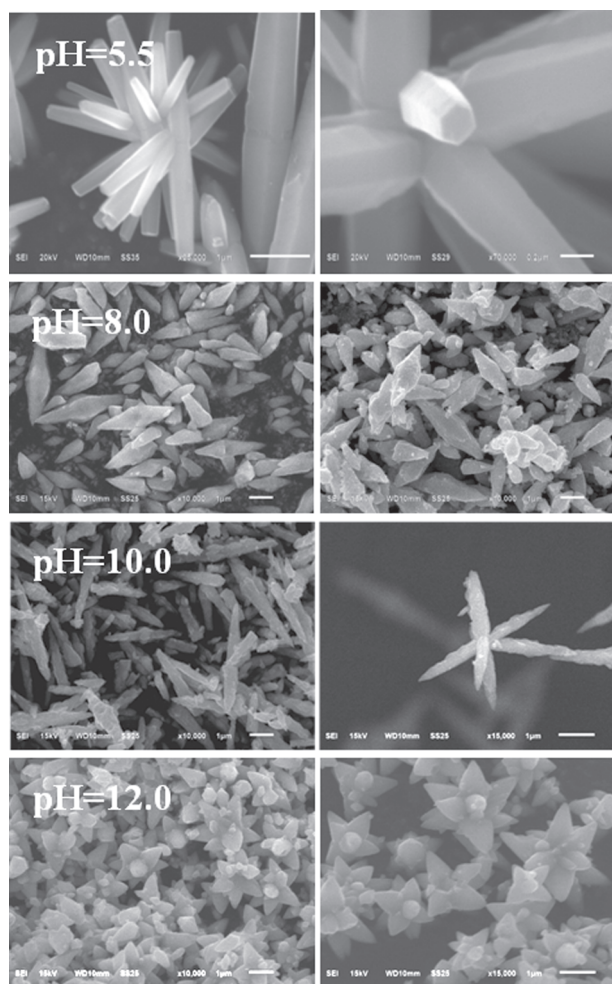
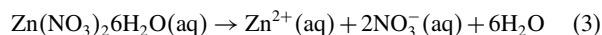
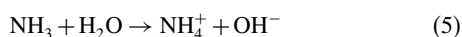


Fig. 3. Typical SEM images of the ZnO nanostructures synthesized at different pH values of the reaction mixture. The images at the right column are of the same sample as that of left column, but taken at higher magnification. The scale bars of all the micrographs are of 1 μm .

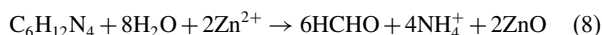
of the reaction mixture. In aqueous medium, zinc nitrate dissociates following the reaction:



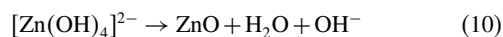
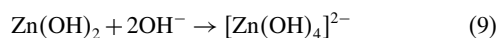
On the other hand, HMT dissociates to form formaldehyde and ammonia in aqueous solution. In presence of free Zn^{2+} ions in the aqueous medium, there occur several reactions in the mixture solution as presented below:



Therefore, the interaction of HMT with the Zn^{2+} ions generated by zinc nitrate precursor in aqueous medium can be written as:



In highly basic medium, the $\text{Zn}(\text{OH})_2$ formed by the reaction of zinc nitrate and HMT (Eqs. (4–6)), reacts with the excess hydroxyl ions to form ZnO according to the reactions:



which are accelerated at elevated temperatures.

The formation of rod-like nanostructures at lower pH value can be understood considering the polar nature of the ZnO crystal lattice and its interaction with HMT. The HMT is a tetradentate ligand which tends to coordinate with metal ions in different ways.³⁵

Due to its non-polar nature, HMT coordinates with the non-polar faces (10-10) and (110-2) of ZnO nuclei without affecting the surface energy of the polar faces (0001) and (000-1) with zinc and oxygen termination, respectively. Therefore, the polar (0001) face grows faster and consequently the nanostructure grows preferentially along the [001] direction (Fig. 3).³⁶ Rod-like ZnO nanostructures have been reported by Tong and collaborators³⁷ using HMT as chelating agent (bonding amino group with zinc ions) and hydrolyzing agent (as the source of OH^- ions) both, where the zinc-amino complex gets absorbed on the lateral faces of ZnO to facilitate the growth in one direction.

On increasing the pH of the reaction mixture (by adding NaOH solution), the molar ratio of Zn^{2+} and OH^- changes, consequently changing the velocity of nucleation and growth, forming nanostructures of other morphologies.³⁸ At higher pH values (>7.0), the ratio of OH^- and Zn^{2+} ion concentration increases, and the growth unit changes.³⁹ Formation of flower-like ZnO nanostructures through hydrothermal synthesis has been reported by Zang et al.⁴⁰ According to them, while the $\text{Zn}(\text{OH})_2$ constitute the nucleation units (Eq. (6)), the $[\text{Zn}(\text{OH})_4]^{2-}$ ions (Eq. (9)) act as growth units, during the nucleation and growth process of the nanostructures, respectively. At moderate basic condition of the reaction mixture, large quantities of zinc hydroxide nuclei are produced, while the number of growth units is small. During the microwave heating, the quantity of ZnO nuclei is large, but there are not enough growth units available for the growth of ZnO nuclei at the reaction temperature ($\sim 95^\circ\text{C}$). On the other hand, there are not many active sites around the ZnO nuclei at this low reaction temperature. Therefore, as the reaction proceeds, the formed nuclei with limited growth rate can get attached together along the preferential direction to form linear (1D) nanostructures as can be seen in the Figure 3, for the pH values 8.0 and 10.0.

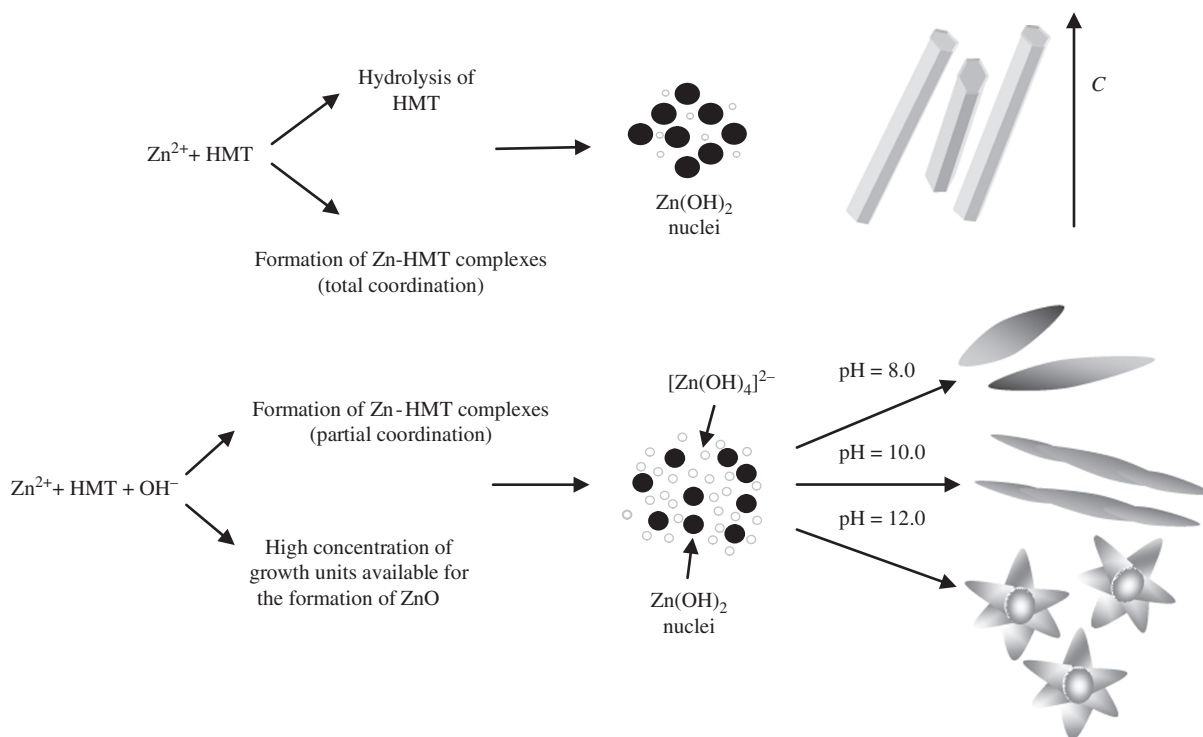


Fig. 4. Schematic presentation of the growth steps of the ZnO nanostructures of different morphologies.

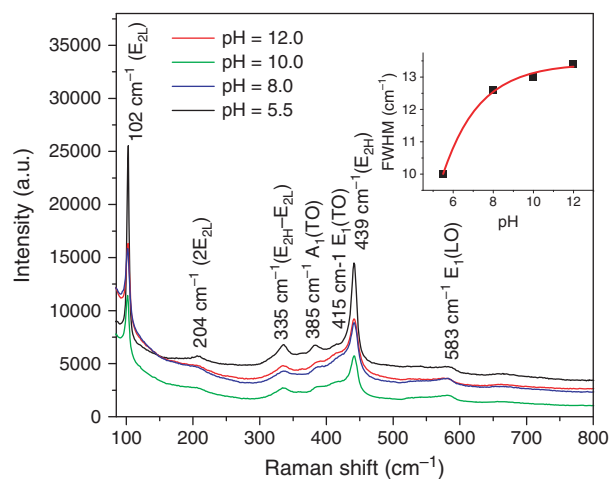


Fig. 5. Room temperature Raman spectra of the ZnO nanostructures synthesized at different pH values of the reaction mixture. The inset shows the variation of FWHM of the E_{2H} band with the pH value of the reaction mixture.

However, at even higher pH values, e.g., pH = 12.0, more a lot of zinc hydroxide units get transformed to $[Zn(OH)_4]^{2-}$ and the number of growth units in the reaction mixture becomes higher than the number of nuclei. Furthermore, at this condition, the number of active sites around the ZnO nuclei increases. Such conditions limit the linear growth of the formed ZnO nuclei and enhance the growth of the nanostructure at the active sites (at the surface), evolving the flower-like morphology. The growth process of the ZnO nanostructures of different morphologies can be understood better from the schematic representation of the growth steps as depicted in the Figure 4.

Raman spectroscopy of the ZnO nanostructures of different morphologies has been carried out to study their vibrational properties. As wurtzite ZnO has C_{6v} ($P6_3mc$) point group symmetry, group theory predicts its optical phonon modes at the Γ point of the Brillouin zone (BZ) through the irreducible representation:

$$\Gamma_{opt} = 1A_1 + 2B_1 + 1E_1 + 2E_2 \quad (11)$$

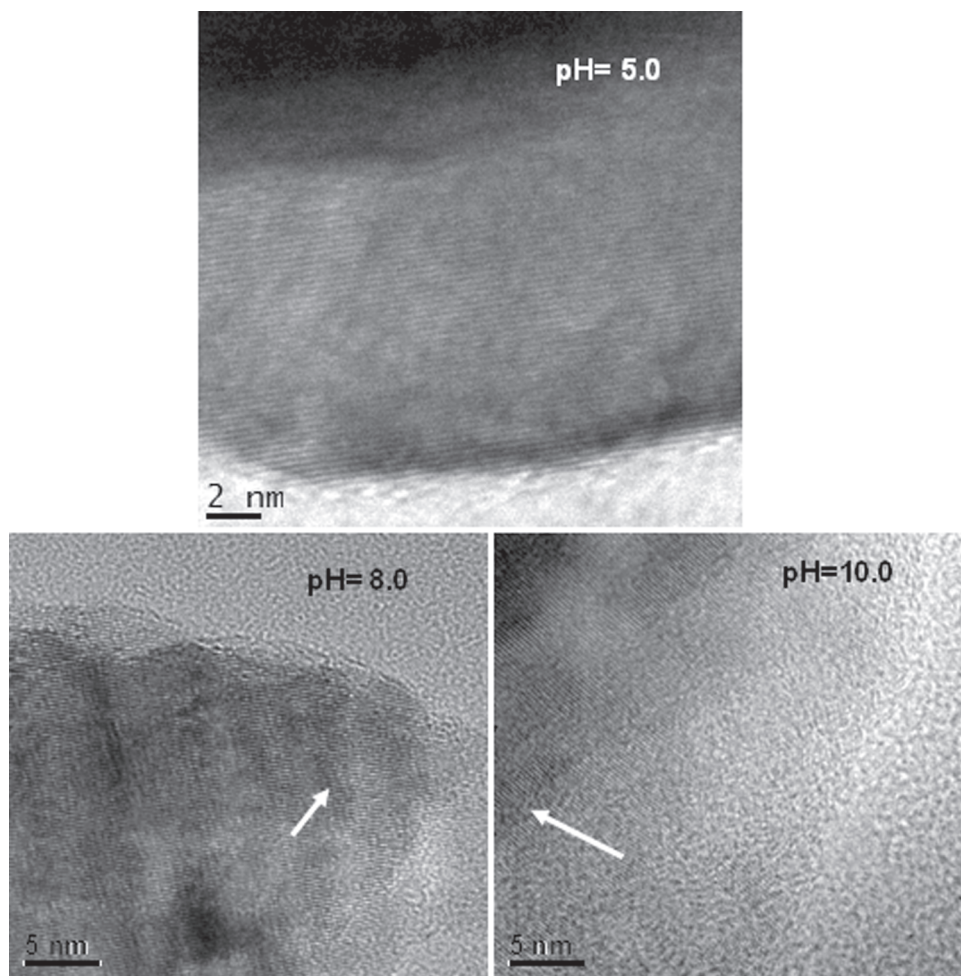


Fig. 6. Typical HRTEM images of the nanostructures grown at different pH values. Loss of crystallinity and introduction of lattice distortion in the nanostructures (shown by arrows) on increasing pH value can be clearly observed from the images.

Both A_1 and E_1 are polar modes and split into transverse optical (TO) and longitudinal optical (LO) components due to macroscopic electric fields associated with the LO phonons.⁴¹ While A_1 and E_1 modes are both Raman and IR active,⁴² the two non-polar E_2 modes (E_{2L} and E_{2H}) are only Raman active. The low frequency mode E_{2L} is associated with the vibration of zinc sub-lattice, and the high frequency mode E_{2H} is associated with the vibration of the oxygen sub-lattice. The two B_1 modes are both infrared and Raman inactive, and are so-called silent modes.⁴³

Figure 5 presents the Raman spectra of the ZnO nanostructures in the 90–800 cm^{-1} spectral range. As can be observed, all the spectra revealed seven Raman peaks located at about 102, 204, 335, 385, 415, 439, and 583 cm^{-1} . The peaks located at 102, 385, 415, 439, and 583 cm^{-1} correspond to the E_{2L} , $A_1(\text{TO})$, $E(\text{TO})$, E_{2H} and $E_1(\text{LO})$ modes of wurtzite ZnO, respectively. The peaks centered at around 204 and 335 cm^{-1} are attributed to the $2E_{2L}$ and ($E_{2H}-E_{2L}$) multi-phonon scattering modes. Finally, the peak appeared around 583 cm^{-1} can be ascribed to the $E_1(\text{LO})$ mode, associated with the defects such as oxygen vacancy, zinc interstitial, or their complexes.⁴⁴

As can be observed, the pH of the reaction mixture strongly affects the intensity and width of the Raman peaks. The effects are most prominent for the E_{2H} mode, located at about 439 cm^{-1} . With the increase of pH of the reaction solution, while the intensity of the Raman peaks decreased, their asymmetric broadening increased. Variation of the full width at half maximum (FWHM) value of the E_{2H} peak with the variation of the pH has been presented as the inset of the Figure 5. Such an increase of FWHM clearly indicates a degradation of crystallinity of the nanostructures with the increase of pH value.⁴⁵ We tried to quantify the asymmetric nature of the Raman peak (E_{2H}) by calculating the asymmetry factor (Γ_a/Γ_b) for the ZnO nanostructures of different morphologies, where Γ_a is the half width at half maximum (HWHM) on the left of the peak position and Γ_b is the HWHM on the right of the peak position. The values of the asymmetry factor for the faceted rods, petals/spindles, twisted-needles and flower-like nanostructures were estimated to be 1.13, 1.45, 1.50, and 1.68, respectively. In general, asymmetry of the Raman peaks has been associated to the presence of defects in semiconductors.⁴⁶ However, Falkovsky⁴⁷ has associated the broadening of E_{2H} mode to the phonon interaction with defects. The broadening is larger on the low frequency side than on the high frequency side of the E_{2H} mode, which gives the line-shape asymmetry. The increase of structural defects and lattice distortion on increasing pH value as has been discussed earlier, could also be observed from the HRTEM images of the samples (Fig. 6).

Room temperature PL spectra of the ZnO nanostructures recorded using 325 nm excitation are presented in Figure 7. The PL spectrum of the rod-like nanostructures (grown at pH = 5.5) revealed two prominent bands. The band appeared in the ultra violet (UV) region (around 385 nm or 3.22 eV) is the commonly known as near band-edge emission, associated to the recombination of free exciton (FX).^{48–51} The broad and intense emission band appeared around 583 nm (2.13 eV) is the visible emission, which is associated to several defect states in the electronic band gap of ZnO. For the obvious reason, this broad band is the superposition of several sub-bands, each of which is associated to a particular defect state in the band gap. Frequently, five sub-bands named blue (~2.60 eV), green (~2.40 eV), yellow (1.95 eV),

orange (2.20 eV) and red (~1.75 eV) emissions are considered as the components of the visible emission in ZnO. Though the origins of these component bands are still controversial, the green emission is frequently associated to the oxygen vacancy

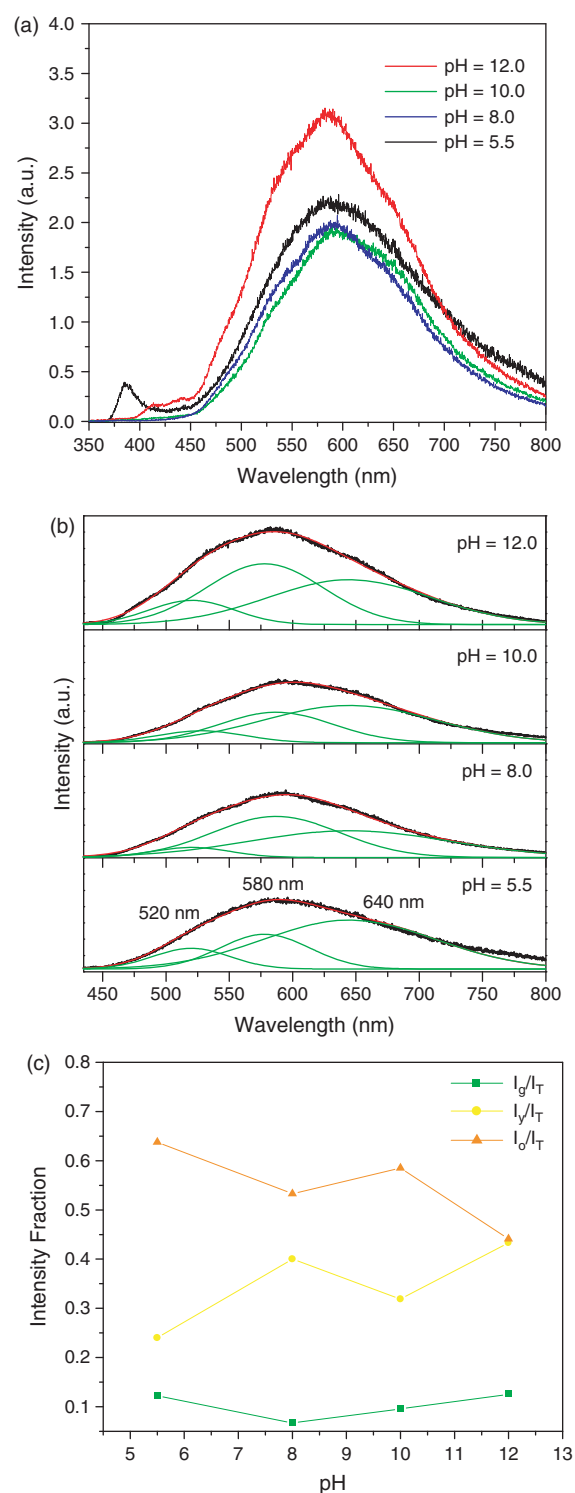


Fig. 7. (a) Room temperature PL spectra of the ZnO nanostructures synthesized at different pH values, (b) computer deconvoluted visible emission band of the nanostructures, and (c) variation of intensity fraction of each of the component bands with the pH values of the reaction mixture.

(V_O^+).^{52–55} As the yellow and orange emissions frequently appear together, it is feasible that they have common defect origins. Nevertheless, their origins remain uncertain.

Interstitial zinc (Zn_i) and singly ionized interstitial oxygen (O_i^-) were proposed^{52,53} as their origins. In oxygen-rich samples, like that prepared in the present work or synthesized by hydrothermal methods, interstitial oxygen is the predominant defect, which forms a deep acceptor level. On the other hand, the origins of red and blue emissions are very much controversial and unclear. They are believed to be associated with the shallow V_O and Zn_i levels, respectively.^{50,56} Out of the five probable emissions, only three contributed in the visible emission in our samples (Fig. 7(b)). Since the same component emission bands appeared for all the samples (though with different intensities), we can assume that they are not dependent on the morphology of the nanostructures.

As can be seen in Figure 7, on increasing the pH of the reaction mixture, the intensity of the UV emission gradually decreases, shifts towards lower energy and finally disappears, probably due to incorporation of shallow levels below the conduction band, resulting from the incorporated structural defects. On the other hand, the intensity and shape of the visible emission band vary with the variation of pH. As the PL spectra of the samples were measured using the nanostructures in powder form, a direct comparison of visible emission intensity is not considered worthy. Therefore, a computer deconvolution was performed to extract the component bands of the visible emission. We could extract three component bands of the visible emission centered at about 520 (2.38 eV), 580 (2.14 eV), 645 (1.92 eV), which correspond to the commonly known green, yellow, and orange emissions in ZnO, respectively. It has been observed that the intensity fraction ($I_{\text{component}}/I_{\text{total}}$) of each of the component bands vary with the variation of the pH of the reaction mixture. In Figure 7(c), the variations of intensity fraction of the component bands with pH of the reaction mixture are presented. As can be noticed, on increasing the pH of the reaction mixture, though the intensity fraction of the green component does not vary substantially, the intensity fractions of the yellow and orange components decreased and increased, respectively. Such an opposite trend of the yellow and orange components clearly demonstrates their different origins, as also suggested by Djuric et al.⁵⁴ Due to the presence of both yellow and orange component bands in our samples with broader and intense yellow component, exact determination of their peak positions is quite difficult by exciting the sample with a particular wavelength. However, the disappearance of the FX emission from the PL emission of the samples prepared at higher pH values indicates the presence of high defect content in them. Evaluation of specific surface area of the nanostructures and their performance in DSSC are in progress.

4. CONCLUSIONS

In conclusion, ZnO nanostructures of well defined morphologies could be produced by microwave assisted chemical synthesis at relatively low temperature by controlling the pH of the reaction mixture. By manipulating the ratio of nucleation and growth units in the solution mixture, nanostructures of rod-like, spindle/petal, twisted-needle, and flower-like morphologies could be synthesized. Highly basic condition of the reaction mixture

produces nonstoichiometric nanostructures, incorporating several defect levels in the energy band gap of ZnO. The defect content in the nanostructures grown by microwave-assisted chemical synthesis depends on the reaction conditions rather than their morphologies.

Acknowledgments: The authors are thankful to CUV-BUAP for extending the SEM and XRD facilities used for this investigation. The work has been partially supported by VIEP-BUAP, through the project grant 2011.

References and Notes

- S. Singh, P. Thiyagarajan, K. M. Kant, D. Anita, S. Thirupathiah, N. Rama, B. Tiwari, M. Kottaisamy, and M. S. R. Rao, *J. Phys. D: Appl. Phys.* 40, 6312 (2007).
- W. Z. Xu, Z. Z. Ye, Y. J. Zeng, L. P. Zhu, B. H. Zhao, L. Jiang, J. G. Lu, H. P. He, *Appl. Phys. Lett.* 88, 173506 (2006).
- C. Y. Jiang, X. W. Sun, G. Q. Lo, and D. L. Kwong, *Appl. Phys. Lett.* 90, 263501 (2007).
- W. I. Park and G.-C. Yi, *Appl. Phys. Lett.* 82, 4358 (2004).
- M. S. Spencer, *Topics in Catalysis* 8, 259 (1999).
- S. Kumar, V. Gupta, and K. Sreenivas, *Nanotechnology* 16, 1167 (2005).
- C. C. Li, Z. F. Du, L. M. Li, H. C. Yu, Q. Wan, and T. H. Wang, *Appl. Phys. Lett.* 9, 32101 (2007).
- S.-H. Nam, S. H. Jeong, and J.-H. Boo, *J. Nanosci. Nanotechnol.* 11, 1648 (2011).
- Y. Zhang and J. Mu, *Nanotechnology* 18, 1 (2007).
- W. L. Hughens and Z. L. Wang, *Appl. Phys. Lett.* 82, 2886 (2003).
- L. Liao, H. B. Lu, M. Shuai, J. C. Li, Y. L. Liu, C. Liu, and Z. X. Shen, *Nanotechnology* 19, 175501 (2008).
- D. P. Singh, *Sci. Adv. Mater.* 2, 245 (2010).
- G. W. Ho, *Sci. Adv. Mater.* 3, 150 (2011).
- D. Chu, Y. Masuda, T. Ohji, and K. Kato, *Langmuir* 26, 2811 (2010).
- M. Willander, P. Klason, L. L. Yang, S. M. Al-Hill, Q. X. Zhao, and O. Nur, *Phys. Stat. Sol. S*, 3076 (2008).
- W. J. E. Beek, M. M. Wienk, and R. A. Jansen, *Adv. Mater.* 16, 1009 (2004).
- C. Y. Jiang, X. W. Sun, G. Q. Lo, and D. L. Kwong, *Appl. Phys. Lett.* 90, 263501 (2007).
- C. Cheng, Y. Shi, C. Zhu, W. Li, L. Wang, K. K. Fung, and N. Wang, *Phys. Chem. Chem. Phys.* 13, 10631 (2011).
- E. Guillén, J. Idígoras, T. Berger, J. A. Anta, C. Fernández-Lorenzo, L. R. Alcántara, J. Navas, and J. Martín-Calleja, *Phys. Chem. Chem. Phys.* 13, 207 (2011).
- G. Koo, W. Lee, B. Kil, H. Ahn, B. W. Cho, and S.-H. Han, *J. Nanosci. Nanotechnol.* 11, 4476 (2011).
- X. Liu, W. H. Cao, and R. P. H. Chang, *J. Appl. Phys.* 95, 3141 (2004).
- H. W. Liang, Y. M. Lu, D. Z. Shen, B. H. Li, Z. Z. Zhang, and C. X. Shan, *Sol. St. Commun.* 137, 182 (2006).
- T. B. Hur, Y. H. Hwang, and H. K. Kim, *J. Korean Phys. Soc.* 46, 120 (2005).
- Ch. H. Ku, H. H. Yang, G. R. Chen, and J. J. Wu, *Cryst. Growth & Des.* 8, 283 (2008).
- A. E. Morales, U. Pal, and M. H. Zaldivar, *J. Nanosci. Nanotechnol.* 8, 6551 (2008).
- H. Van den Rul, D. Mondelaers, M. K. Van Bael, and J. Mullens, *J. Sol-Gel Sci Technol.* 39, 41 (2006).
- J. Wu and D. Xue, *Sci. Adv. Mater.* 3, 127 (2011).
- A. G. Leyva, P. Stoliar, M. Rosenbusch, V. Lorenzo, P. Levy, C. Albonetti, M. Cavallini, F. Biscarini, H. E. Troiani, J. Curiale, and R. D. Sanchez, *J. Sol. St. Chem.* 177, 3949 (2004).
- A. M. Peiro, J. A. Ayllon, J. Peral, X. Domenech, and C. Domingo, *J. Cryst. Growth* 285, 6 (2005).
- M.-Q. Zhu, T. Zhao, M. Zhu, J.-B. Fan, G.-C. Chen, and Z. W. Liang, *Chem. Com.* 47, 3986 (2011).
- S. D. Gopal Ram, M. A. Kulandainathan, and G. Ravi, *Appl. Phys. A* 99, 197 (2010).
- L. Zhang and Y.-J. Zhu, *Appl. Phys. A* 97, 847 (2009).
- I. Bilecka, L. Luo, I. Djerdj, M. D. Rossell, M. Jagodic, Z. Jaglicic, Y. Masubuchi, S. Kikkawa, and M. Niederberger, *J. Phys. Chem. C* 115, 1484 (2011).
- J. J. Schneider, R. C. Hoffmann, J. Engstler, E. E. Klyszcz, P. Jakes, R.-A. Eichel, L. Pitta-Bauermann, and J. Bill, *Chem. Mater.* 22, 2203 (2010).
- H. Jiang, J. Hu, F. Gu, and C. Li, *Nanotechnology* 20, 55706 (2009).
- A. Sungunan, H. C. Warad, M. Boman, and J. Dutta, *J. Sol-Gel. Sci. Technol.* 39, 49 (2006).

37. Y. Tong, Y. Liu, L. Dong, D. Zhao, J. Zhang, Y. Lu, D. Shen, and X. Fan, *J Phys Chem. B* 110, 20263 (2006).
38. U. Pal and P. Santiago, *J. Phys. B* 109, 15317 (2005).
39. W. Y. Wu, W. Y. Kung, and J. M. Ting, *J. Am. Ceram. Soc.* 94, 1 (2010).
40. H. Zhang, D. Yang, X. Ma, Y. Ji, J. Xu, and D. Que, *Nanotechnology* 15, 622 (2004).
41. A. Escobedo-Morales and U. Pal, *Current Appl. Phys.* 11, 525 (2011).
42. H. W. Suh, G. Y. Kim, Y. S. Jung, and W. K. Choi, *J. Appl. Phys.* 97, 44305 (2005).
43. V. Pachauri, C. Subramaniam, and T. Praddep, *Chem. Phys. Lett.* 423, 240 (2006).
44. W. Peng, S. Qu, G. Cong, and Z. Wang, *Cryst. Growth & Des.* 6, 1518 (2006).
45. D. Vernardu, G. Kemamakis, S. Couris, E. Koudoumas, E. Kymakis, and N. Katsarakis, *Thin solid films*, 515, 8764 (2007).
46. Y. Y. Tay, T. T. Tan, M. H. Liang, F. Boey, and S. Li, *Appl. Phys. Lett.* 93, 111903 (2008).
47. L. A. Falkovsky, *Phys. Rev. B* 64, 24301 (2001).
48. B. D. Yao, Y. F. Chan, and N. Wang, *Appl. Phys. Lett.* 81, 757 (2002).
49. X. Zhang, Y. Zhang, J. Xu, Z. Wang, X. Chen, D. Yu, P. Zhang, H. Qi, and Y. Tian, *Appl. Phys. Lett.* 87, 123111 (2005).
50. X. Q. Wei, B. Y. Man, M. Liu, C. S. Xue, H. Z. Zhuang, and C. Yang, *Physica B* 388, 145 (2007).
51. A. Escobedo-Morales and U. Pal, *Appl. Phys. Lett.* 93, 193120 (2008).
52. E. De la Rosa, S. Sepúlveda-Guzmán, B. R. Jayan, A. Torres, P. Salas, N. Elizondo, and J. M. Yacamán, *J. Phys. Chem. C* 111, 8489 (2007).
53. X. L. Wu, G. G. Siu, C. L. Fu, and H. C. Ong, *Appl. Phys. Lett.* 78, 2285 (2001).
54. A. B. Djuricic, Y. H. Leung, K. H. Tam, L. Ding, W. K. Ge, H. Y. Chen, and S. Gwo, *Appl. Phys. Lett.* 88, 103107 (2006).
55. A. Escobedo-Morales, R. Aceves, U. Pal, and J. Z. Zhang, *J. Nanosci. Nanotechnol.* 8, 6538 (2008).
56. J. H. Cai, G. Ni, G. He, and Z. Y. Wu, *Phys. Lett. A* 372, 4104 (2008).

Received: xx Xxxx xxxx. Accepted: xx Xxxx xxxx.